Flow Characteristics and Vortex Structure of Flow Across Micro Cylinders by Micro-PIV Measurement and CFD Simulation

M. Liu, M. Tao, Y. Kang [†] and D. Gao

School of Mechanical and Electrical Engineering, Kunming University of Science and Technology Kunming, Yunnan Province, 650093, China

†*Corresponding Author Email: yuchi.kang@kust.edu.cn*

ABSTRACT

The micro tube bank model is a commonly used structure in microelectro mechanical cooling systems. Flow across a micro tube bank is a basic benchmark for analyzing flow resistance and heat transfer capability. In this paper, the flow around a micro tube bank model was studied both experimentally and numerically. Micro-Particle Image Velocimetry technology was used to measure the flow field at different inlet flow rates. The laminar flow model, S-A model and standard k-ε model were used to calculate the flow field inside the micro tube bank model. By comparing the results from the three numerical models with the experimental results, there is a certain gap between them can be noted. However, it was found that the standard k-ε model is better than laminar model and S-A model in the comparison between numerical results and experimental results. In conclusion, the standard k-ε model is more suitable for the numerical calculation of the flow field around a micro scale tube bank model.

Keywords: Fluid flow; Micro cylinders; Micro-PIV; Numerical simulation; Vortex.

NOMENCLATURE

A	cross sectional area	Re	Reynolds number
C_1, C_2, C_3	empirical constants	S	strain rate tensor
Cp	specific heat	S_T, S_L, S_D	spacing distance
C_μ	experience factor	$S_k. S_\varepsilon$	user-defined source term
Cy	force coefficient in the y direction	T	temperature
d	diameter	V	velocity component
f	vector of forces acting	u, v, w	velocity in x, y, z
G_b	turbulent kinetic energy from buoyancy	Y_M	influence term for pulsating expansion in compressible turbulence.
G_k	turbulent kinetic energy from laminar velocity gradients	Y_v	reduction in turbulent viscosity
G_v	turbulent viscosity generating term	ρ	density
k, σ_v, C_{b1}	constant	μ	dynamic viscosity
N_L, N_T	number of microcylinders	λ	viscosity coefficients
P	constant pressure	ε	turbulent dissipation rate
Q	flow velocity	$\sigma_k, \sigma_\varepsilon,$	corresponding Prandtl number

1. INTRODUCTION

With the continuous growth of numerical computing capability, a significant amount of heat is generated by electronic chips, leading to a service life reduction. Studies have shown that when the temperature of electronic components rises by 10°C, the service life is only half that of the original; when the temperature exceeds the load-bearing limit, permanent damage such as thermal breakdown can occur (Hosseinizadeh *et al.* 2011; Kumar *et al.* 2021a,b). To ensure long-term stable operation, thermal structures, such as heat sink, need to be incorporated in electronic components and equipment (Wang *et al.* 2021). A micro tube bank model is a typical geometry in thermal structures (Xu

et al. 2005; Shah *et al* 2022; Siddiqui *et al.* 2022). A micro tube bank model is composed of multiple micro cylinders that alter the direction of fluid flow and create vortices when the fluid passes through (Paramanantham *et al.* 2022). As a classical physical model for scholars to study the micro heat sink, it is important to study its internal bypass flow characteristics further to help improve the heat transfer performance.

With the development of Micro-Particle Image Velocimetry technology (Micro-PIV), researchers have shown an increased interest in experimental investigation into flow across micro cylinders and micro tube bank models. (Armellini *et al.* 2010; Stogiannis *et al.* 2014).

Some scholars have studied flow across a micro cylinder using Micro-PIV, they have found that the critical Reynolds number (Re) is 10 for vortex appearance. With an increasing Re, the length of the cylindrical wake region, the scale of the vortex, and the vortex intensity rise. When Re reaches 400, the vortex begins to appear to shed. As Re continues to increase, the formation of a Carmen vortex street has been found at the rear of the micro cylinder (Ji *et al.* 2021; Li *et al.* 2020; Wang *et al.* 2020).

Fluid flow across micro tube bank models has been widely analyzed since the micro tube bank is a common structure in heat transfer. By analyzing the vortex structure, velocity distribution, and pressure drop, it can be found that when Re is 100, the flow separation phenomenon occurs in the middle cylinder of the micro tube bank model. When Re is 150, vortices appear in the wake region; when Re is less than 200, the flow is stable. As Re increases, the internal flow starts to turn, and the pressure drop decreases significantly. When Re is 250, symmetrical vortices appear in the wake region. Cylinder arrangement is an important factor in flow patterns. With a staggered arrangement micro tube bank model, the velocity and shear stress distribution show periodic changes along the flow and diffusion directions. Additionally, vortex emergence and shedding of a staggered arrangement micro tube bank model occurs at a lower Re than that of an in-line arrangement. The velocity distribution in an in-line arrangement micro tube bank model is more uniform than that in a staggered arrangement. (Renfer *et al.* 2011; Li *et al.* 2018; Liu *et al.* 2021).

The cross-section geometry of a cylinder is found to be influential in fluid flow across a micro tube bank. A diamond-shaped micro tube bank model can produce a vortex at a lower Re than a circle-shaped one. (Liu *et al.* 2019; Qin *et al.* 2019; Zhu *et al.* 2017).

Consequently, it can be found that the experimental study of cylindrical winding flow at microscale depends on the development of microscopic techniques and experimental devices, and the current experimental study of micro tube bank models mainly focuses on vortex, and further research and analysis into the flow details inside a micro tube bank model are required.

The published numerical calculations on micro tube bank models are mainly focused on heat transfer, and the flow characteristics, but specific details about its interior are less studied. In these numerical calculations, different numerical models are calculated by commercial code Fluent, most commonly used are the laminar flow model, the Spalart-Allmaras turbulence model, the standard *k-ε* model, Renormalization-group model and Lattice Boltzmann model. Numerical simulations have demonstrated that adding a micro tube bank model within a micro heat sink can substantially improve the heat transfer efficiency compared to microchannels (Jia *et al.* 2018). Different numerical models are suitable for different Re conditions; in addition, through the numerical calculation studies of different shapes of micro tube bank model, it has been found that different micro-column shapes within micro heat sinks play an important role in equilibrium pressure drop and heat transfer efficiency (Ambreen and Kim 2018; Cai *et al.* 2016; Shafeie *et al.* 2013). However, in the numerical calculation of the micro tube bank model, there are fewer comparative studies for different numerical models under the same conditions, and the vast majority of the studies are more oriented to the study the overall performance. The internal flow pattern study still needs further investigation.

By analyzing the progress of experimental and numerical calculations of the micro pin fin array model, it can be seen that scholars at home and abroad have conducted investigations and achieved promising results, but both experiments and numerical calculations mainly focus on the overall performance, such as drag and heat transfer characteristics, and the research on specific internal flow details is insufficient. In this paper, the experimental and numerical investigation into fluid flow across micro tube bank models were conducted to study the velocity distribution and flow pattern in detail. The aim of this study is to find a suitable numerical model which is able to predict flow across micro tube bank models. The present research is a theoretical basis for future work about heat transfer and drag characteristics in micro heat sinks.

2. EXPERIMENTAL SETUP

Micro tube bank models are adopted in the present paper. Experiments are carried out on microfluidic devices made from polydimethylsiloxane (PDMS). A schematic view is presented in Fig. 1. Built-in cylinders are arranged in a stagger manner in PDMS channels. There are four columns in the vertical
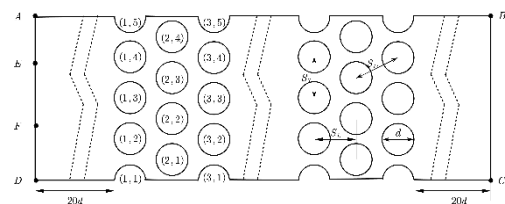

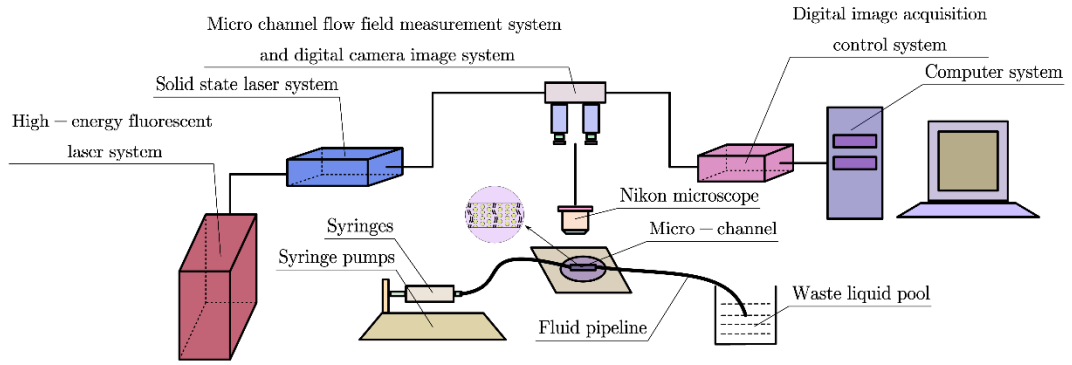**Fig. 1. Schematic diagram of a micro tube bank model PDMS channel.**

Fig. 2. Microscopic particle image velocimetry system.

Table 1 Geometry parameters for micro tube bank mode.

d(mm)	S_T/d	S_L/d	S_D/d	N_L	N_T
0.4	1.5	3	3.354	16	4

direction at a distance of S_t=1.5d and sixteen columns in the horizontal direction at a distance of S_l=3d. The diameter of the cylinder is 0.4 mm. To ensure the flow is fully developed as it enters and exits the interfaces, the flow channel is extended to 20 times the diameter of the cylinder upstream and downstream. Detailed parameters are listed in Table 1.

The velocity distribution was measured with the Micro-PIV system, which is schematically presented in Fig. 2. The experimental setup mainly consists of a high-energy fluorescent laser system (SM3-FL200), a solid-state laser system, a micro-channel flow field measurement system (SM3-MICROFLOW), a digital camera image system (SM- CCDB5M16), a Nikon microscope, microchannels, a syringe, a syringe pump (Pump 11 Elite, Harvard Apparatus, shown in Fig. 3), a waste pool, a digital image acquisition a system, control system (sm3-imagecap) and a computer display system.

As the micro tube bank channels used in experiments are at the micro-level, tracer particles for macroscopic PIV experiments are not applicable. In this paper, Nile red tracer particles with a nominal diameter of 1 μm were selected. The concentration of tracer particle solution was 1.8%. To avoid aggregation, the tracer particle solution was treated
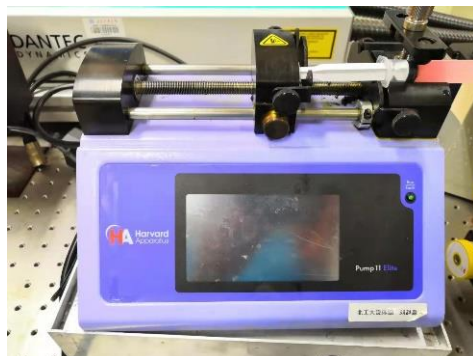

Fig. 3. Photo of Pump 11 Elite.

by ultrasonic processing prior to the experiments. Given that flow rates in a Micro-PIV measurement ranges between μL and ml, a higher precision driving unit is essential. In the present research, the range was set at 1.28 μL /min - 25.99 ml /min, with an accuracy of ±0.5%, to meet the experimental requirements. A polypropylene medical syringe was not installed in the present research, since invisible deformation may occur at the syringe barrel, and this may have negative effects on experimental outcomes. A Hamilton 1000LTN glass syringe from Harvard Apparatus was used; this is made of hard glass and filled with polytetra-fluoroethylene (PTFE) as the seal between the plunger flange and the barrel, with a capacity of 1 ml. A rigid 0.5 mm-diameter capillary (Labsmith) made of polyetheretherketone (PEEK) was used to connect the syringe to the channel. The acquired tracer particle images needed to be post-processed. The capture tracer particle images were processed using Dynamic Studio software on a working station. A cross-correlation algorithm was applied to investigate the velocity distribution.

3. CFD NUMERICAL MODEL

3.1 Mathematical Models

a) Governing Equations

Continuity equation (Saravanan and Umesh 2018):

$$\frac{\partial}{\partial x_i}(\rho u_i) = 0 \tag{1}$$

where ρ is fluid density, and u_i is the velocity of motion of the fluid.

Momentum equations:

$$\frac{\partial}{\partial x_i}(\rho u_i u_k) = \frac{\partial}{\partial x_i}(\mu \frac{\partial u_k}{\partial u_i}) - \frac{\partial p}{\partial x_k} \tag{2}$$

where μ is dynamic viscosity, and P is stress tensor.

Energy equation:

$$\frac{\partial}{\partial x_i}(\rho u_i T) = \frac{\partial}{\partial x_i}(\frac{k}{c_p}\frac{\partial T}{\partial x_i}) \tag{3}$$

where c_p is specific heat capacity, k is thermal conductivity, and T is temperature.

b) Control Equations for the S-A Model

The Spalart-Allmaras (S-A) turbulence model is a one-equation turbulence model, which gives satisfactory numerical outcomes in many practical applications, such as fluid close to a wall, where viscous effects dominate. The S-A model is premised on the assumption that the local Reynolds stress tensor is considered to be proportional to the gradient of the mean velocity. The transport equation is given by (Lee *et al.* 2018):

$$\rho \frac{D\overline{v}}{Dt} = G_v + \frac{1}{\sigma_{\overline{v}}} [\frac{\partial}{\partial x_j} \{(\mu + \rho \overline{v}) \frac{\partial \overline{v}}{\partial x_j}\} + C_{b2} \left(\frac{\partial \overline{v}}{\partial x_j}\right)^2] - Y_v \tag{4}$$

where $\overline{v}$ stands for the viscosity coefficient of turbulent motion, v stands for the viscosity coefficient of molecular motion; G_v is a generated item, and Y_v is a broken item.

$$G_v = C_{b1} \rho \overline{S} \overline{v} \tag{5}$$

$$\overline{S} \equiv S + \frac{\overline{v}}{k^2 d^2} f_{v2} \tag{6}$$

$$f_{v2} = 1 - \frac{x}{1 + x f_{v1}}, S \equiv \sqrt{2\Omega_{ij}\Omega_{ij}} \tag{7}$$

$$S \equiv \sqrt{\Omega_{ij}\Omega_{ij}} = \frac{1}{2}\left(S \frac{\partial u_j}{\partial x_i} - \frac{\partial u_i}{\partial x_j}\right) \tag{8}$$

$$Y_v = C_{w1} \rho f_w \left(\frac{\overline{v}}{d}\right)^2 \tag{9}$$

$$f_w = g \left[\frac{1 + C_{w3}^6}{g^6 + C_{w3}^6}\right]^{1/6} \tag{10}$$

$$g = r + C_{w2}\left(r^6 - r\right) \tag{11}$$

$$r \equiv \frac{\overline{v}}{\overline{S} k^2 d^2} \tag{12}$$

Correction formula near the wall:

$$S \equiv \left|\Omega_{ij}\right| + C_{prod} \min\left(0, \left|S_{ij}\right| - \left|\Omega_{ij}\right|\right) \tag{13}$$

where C_{prod}=2.0.

$$\left|\Omega_{ij}\right| = \sqrt{2\Omega_{ij}\Omega_{ij}} \tag{14}$$

$$\left|S_{ij}\right| \equiv \sqrt{2S_{ij}S_{ij}} \tag{15}$$

Coefficient values in the S-A model are:

C_{b1}=0.1335, C_{b2}=0.622, $\sigma_{\overline{v}}$ =1.5, C_{v1}=7.1,

$C_{w1} = C_{b1} / k^2 + \left(1 + C_{b2}\right) / \sigma_{\overline{v}}$, C_{w2}=0.3, C_{w3}=2.0, k=0.41.

c) Control Equations for the Standard *k-ε* Model

The standard *k-ε* model was introduced in 1974 by Launder and Spalding. This model adds the turbulent kinetic energy dissipation rate ε to the turbulent k equation in the one-equation model to form the standard *k-ε* model. The main equations (Shaheed *et al.* 2019; Ejaz *et al* 2022) in this model are as follows:

The transport equations in this model are written as:

$$\frac{\partial k}{\partial t} + \frac{\partial k u_i}{\partial x_i} = \frac{\partial}{\partial x_i}\left(Dk_{eff} \frac{\partial k}{\partial x_i}\right) + G_k - \varepsilon \tag{16}$$

$$\frac{\partial \varepsilon}{\partial t} + \frac{\partial \varepsilon u_i}{\partial x_i} = \frac{\partial}{\partial x_i}\left(D\varepsilon_{eff} \frac{\partial \varepsilon}{\partial x_i}\right) + \sqrt{2}C_{1\varepsilon}S_{ij}\varepsilon - C_{2\varepsilon} \frac{\varepsilon^2}{k + \sqrt{v\varepsilon}} \tag{17}$$

$$v_t = C_\mu \frac{k^2}{\varepsilon} \tag{18}$$

$$C_\mu = \frac{1}{A_0 + A_s \frac{kU^*}{\varepsilon}} \tag{19}$$

$$\frac{\partial \varepsilon u_i}{\partial x_i} U^* = \sqrt{S_{ij}S_{ij} + \tilde{\Omega}_{ij}\tilde{\Omega}_{ij}} \tag{20}$$

$$\tilde{\Omega}_{ij} = \tilde{\Omega}_{ij} - \varepsilon_{ijk}\omega_k - 2\varepsilon_{ijk}\omega_k \tag{21}$$

where A_0=4, $A_s = \sqrt{6} \cos \varphi$.

$$\varphi = \frac{1}{3} \text{Arccos}\left(\min\left(\max\left(\sqrt{6}W, -1\right), 1\right)\right) \tag{22}$$

$$\varepsilon_{ijk}\omega_k W = \frac{S_{ij}S_{jk}S_{ki}}{\tilde{S}^2} \tag{23}$$

$$S_{ij}C_{1\varepsilon} = \max\left(\frac{\eta}{5+\eta}, 0.43\right) \tag{24}$$

$$\eta = S\left(\frac{k}{\varepsilon}\right) \tag{25}$$

The constants C_2, σ_k and σ_ε were defined as:

C_2=1.9, σ_k=1.0, and σ_ε=1.2.

The standard *k-ε* model assumes a fully turbulent flow field, ignoring the effect of viscosity between molecules, and is therefore only applicable to fully turbulent flow fields. The standard *k-ε* model is the most widely used turbulence model in engineering practice because it is popular for its appropriate computer requirements and reasonable accuracy.

3.2 Mesh Generation

Figure 4 presents the grid meshing of a located area around a micro cylinder. According to Tan's research on the grid sensitivity of the tube bank model and considering numerical computational capability (Tan *et al.* 2017), 5 layers of boundary layer grids were separated near the circular surface along the radial direction, and 320 grids were determined along the circumferential direction. Rectangular structural grids were applied. The remainder was meshed with triangular unstructured grids. Figure 5 demonstrates the grid independence verification. The grid independence work was conducted by standard k-ε model at Q2000μL/min. The total number of units is approximately 400000.
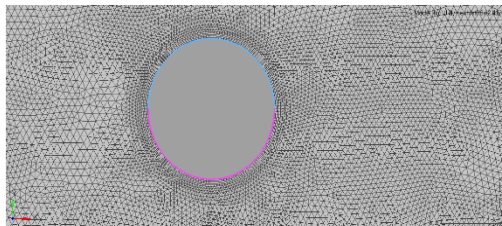

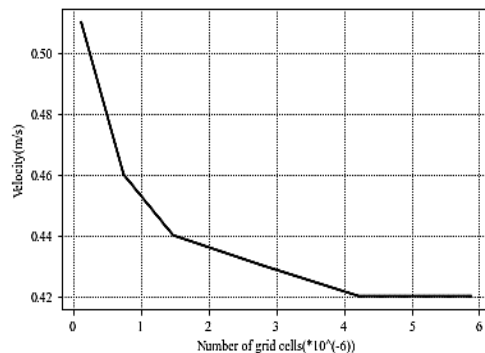**Fig. 4. Grid meshing.**

Fig. 5. Grid independence verification.

3.3 Boundary Condition and Settings

As demonstrated in Fig. 1, EF was set as the velocity inlet, and BC was set as the outlet. The outlet pressure was atmospheric pressure. The other surfaces were set as the standard wall. To ensure the flow was fully developed as it enters and exits the interfaces, the flow channel is extended to 20 times the diameter of the cylinder upstream and downstream.

Water was adopted as fluid medium. The SIMPLE scheme, a pressure-based segregated algorithm, was adopted. The discretization scheme for pressure was the second order. The discretization scheme for momentum and turbulent kinetic energy was the second order upwind. The first order upwind was used to discrete the turbulent dissipation rate term. The solver relaxation factors for the momentum, turbulent kinetic energy and turbulent dissipation rate were 0.7, 1 and 1, respectively, which are default settings.

For ease of description, (x, y) was adopted to denote the location of a cylinder. For example, (1,1) refers to the cylinder in the first row of the first column. (3, 2) refers to the cylinder in the third row of the second column.

Flow rates in this experiment were between 500μL/min-5mL/min. During each shot, the interrogation window of this Micro-PIV system could only cover an area which is slightly larger than the gap between two cylinders. To comprehensively investigate the flow regime around cylinders, repeated experiments were conducted at one flow rate to enable more gaps between the two cylinders to be photographed. To save time, 500μL/min, 2000μL/min, 5000μL/min and 8000μL/min were chosen as flow rates for the experiments.

Re has been frequently adopted to analyze the flow regime inside a micro flow channel. Velocity (expressed in m/s) is necessary in Re calculations. The syringe pump employed was controlled by flow rate (expressed in μL/min). The transformation between velocity and flow rate is as follows:

$$V = \frac{Q}{A} \tag{26}$$

where *V* is the simulation entrance speed, *Q* is the experimental entrance flow rate, and *A* is channel entrance area.

4. COMPARISON OF EXPERIMENTAL AND NUMERICAL RESULTS

Figure 6 shows images of tracer particles in the downstream region of (6, 3) at different inlet flows. To be clearly stated, images were post-processed. The white semicircle represents the micro cylinders. The white spots represent tracer particles. The black areas represent no tracer particles. The images listed were all taken after the flow field was stable. It can be seen from the figure that the tracer particles are evenly distributed in the flow field.
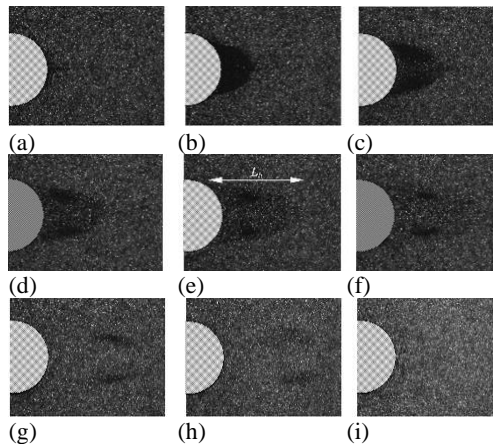
Fig. 6. Seeding particle photos of circle (6,3) downstream area at Q is 2000 (a), 3000 (b), 3500 (c), 4000 (d), 4500 (e), 5000 (f), 8000 (g), 10000 (h) and 15000 (i)μL/min.

4.1 Tracer Particle Image

As demonstrated in Fig. 6(a), when Q is 2000μL/min, the flow separation phenomenon is not found in the downstream area of the cylinder. When Q is 3000μL/min, a black area downstream of the cylinder can be seen, while tracer particles in this area cannot be identified. This proves that flow separation occurs. As the flow rate continues to increase, the black area gradually becomes larger in both the horizontal and vertical directions. The black area is divided into two parts and a gap between the two can be seen when Q is 3500μL/min. This represents significant evidence that the level of flow separation becomes stronger with a larger flow rate. When Q is 8000μL/min, due to the field's limitation of vision, the full length of the vortex can no longer be photographed. When Q is 15000μL/min, the vortex fell off, forming Karmen vortex streets, so there is no vortex image in Fig. 6(i). In the present research, L_h/d was applied to describe the vortex length in a dimensionless manner. L_h is the horizontal distance between the flow separation point and the end of the vortex. Table 2 lists the relationship between L_h and Q when Q ranges from 3000 to 5000. It can be seen that L_h/d becomes gradually larger.

4.2 Comparison of the time-averaged velocity distribution

Figure 7 presents a time-averaged velocity distribution comparison between the experimental results and the laminar flow model results, S-A model results, and standard k-ε model results as the flows around the current of the cylinders (1, 2) and (1, 3) at a flow rate (Q) of 500μL/min. In Fig. 7(a), the velocity distribution in this area presents an
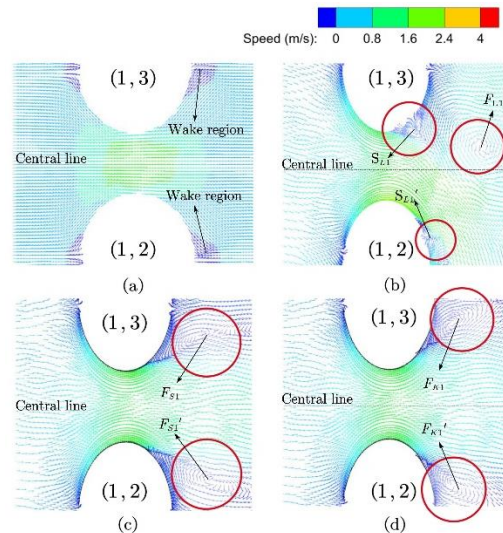

Fig. 7. Area around (1, 2) and (1,3) velocity vector comparison between the experimental results (a) and laminar model results(b), S-A model (c) and standard k-ε model (d) at Q 500μL/min.

uneven distribution flow pattern. The greatest velocity occurs at a point between the two cylinders while the lowest velocity can be found at upstream and downstream regions of the cylinders. The reason for this phenomenon is that the area of fluid flow around the two cylinders is shrunk. There is an inverse proportional relationship between Q and V. So velocity distribution at the gap is the largest. The average velocity distribution at the wake area is symmetrical along the center horizontal line. Due to the low velocity, it can be clearly seen from Fig. 7(a) that there is no flow separation in the downstream wake of the two columns. Figure 7(b) presents the numerical results of the laminar model. It can be seen that velocity distribution at the gap is the largest, while it is smallest upstream and downstream of the cylinders. This is consistent with experimental results. While the velocity distribution in the downstream area is not symmetrically distributed along the central horizontal line. Additionally, the average velocity in the downstream of cylinders (1, 2) is significantly higher than that in the downstream area of cylinders (1, 3).

In Fig. 7(b), two saddle points are indicated by S_{L1} and S_{L1}', and the sub-vortex downstream of cylinder (1, 3) is more mature. In addition to this, it can be noted that the flow separation phenomenon occurs in the downstream region of the cylinder (1, 3), generating a clockwise local point group F_{L1}. By analyzing the F_{L1} velocity vector, it can be found that the vortex is shedding.

Table 2 Relationship between L_h/d, Q, V and Re.

Q (μL/min)	3000	3500	4000	4500	5000
L_h/d	0.523	0.669	0.885	1.039	1.201
V(m/s)	0.694	0.810	0.926	1.042	1.157
Re	277	324	370	416	462

Figure 7(c) presents the numerical results of the S-A model. It can be seen that the velocity is symmetrically distributed around the two cylinders. The maximum velocity occurs at the gap while the minimum velocity occurs at the front and rear part of two cylinders. But one point that should be noticed is that the velocity magnitude is significantly larger than those demonstrated by the experimental results. The maximum value is circa 1.1m/s in the experiments, while it is around 1.9m/s in the S-A numerical results. It can also be noted that flow separation occurs downstream of both cylinders, generating two focal points F_{S1} and F_{S1}' symmetrical to the horizontal centerline of the two cylinders. By analyzing the velocity vector of this focal point group, it can be found that the vortex does not shed and remains adhered to the downstream wall of the cylinders.

The results of the standard k-ε model are very similar to those of the S-A. model, with symmetrical focal points F_{K1} and F_{K1}' in the downstream region of both cylinders. However, the results of both models show that the core of the focal point group of the k-ε model is closer to the cylinder wall, and its vortex separation angle is significantly smaller than that of the S-A model.

In the fluid flow across a cylinder, the generation of the focal point is related to the Re. When the Re is small, no core is generated. When the Re is large, the focal point group is generated on the downstream surface of the cylinder and a focal point is generated, and as the Reynolds number continues to increase, the focal point group is shed, and the saddle point disappears. From Fig. 7, it is evident that the four types of results are different from each other, and this represents four different Re. The experimental Re is the lowest because no flow separation can be found. For the laminar flow model, not only does the flow separation phenomenon appear, but also the shedding of vortices occurs; thus, its Re is the highest. By comparing the relationship between Re and the time-averaged velocity vector distribution of the four models, it can be found that the standard k-ε model is closer to the experiment results.

Figure 8 presents a local area velocity distribution comparison between the experimental results and the laminar flow model results, S-A model results and standard k-ε model results at the working condition of Q of 2000μL/min. In order to better investigate the flow details, the cylinder (6, 3) in the central region of the micro tube bank model was selected to compare the four kinds of results.

From the experimental results, it can be seen that the mean velocity distribution in the wake region of the cylinder (6, 3) is symmetrical to the horizontal line of the center of the cylinder, and no flow separation phenomenon occurs. In contrast, the remaining three models have more obvious foci and flow separation occurs.

From Fig. 8(b), it can be seen that the laminar flow model shows significant flow separation and forms a pair of secondary vortices symmetrical to the horizontal line of the center of the cylinder, whose
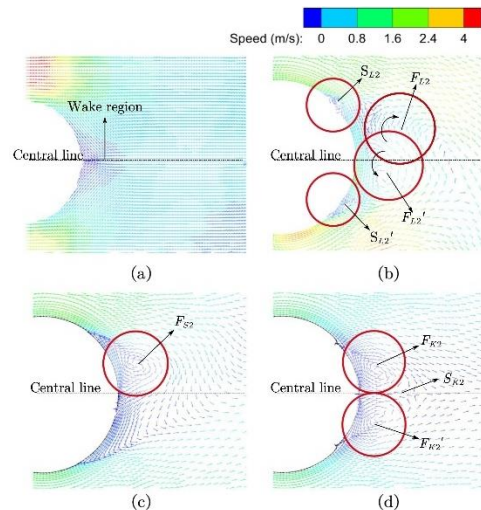

Fig. 8 Area downstream (6, 3) velocity vector comparison between the experimental results (a), laminar model results (b), S-A model (c), and standard k-ε model (d) at Q is 2000μL/min.

secondary saddle points are S_{L2} and S_{L2}', respectively. These can be seen to adhere to the surface downstream of the cylinder (6, 3). It should be noted that the laminar flow model results exhibit a significantly higher velocity in the cylindrical wake region than is the case with the experimental results and the results of the other two models. In addition to the formation of two symmetrical sub-vortices, a focus in the opposite direction is formed downstream of the cylinder, with a clear counterclockwise focus below the horizontal line at the center of the cylinder, with a dislodged one already occurring, while a clockwise immature focus is presented above.

From the S-A model, it can be seen that the time-averaged velocity distribution downstream of the cylinder is not symmetrically distributed to the cylindrical center horizontal line, and a clockwise focus F_{S2} is presented above the cylindrical center horizontal line. From the k-ε model results, it can be seen that a pair of foci F_{K2} and F_{K2}'-symmetrically distributed about the cylindrical center horizontal line-appear downstream of the cylinder (6, 3), and its saddle point is S_{K2}.

A comparison of four types of results shows that for the laminar flow model, all three kinds of numerical results show flow separation phenomena. Laminar flow model results not only show a pair of symmetrical secondary vortices but also produce the shedding of foci. S-A model results also produce the shedding of focus, while the k-ε model results produce a pair of symmetrical foci but no shedding occurs. Both experimental results and standard k-ε model results present similar data although with slight differences. Therefore, the standard k-ε model is better able to predict the flow across micro tube bank model.

Figure 9 and Fig. 10 show the time-averaged velocity distribution comparison between the experimental results and numerical results for the working
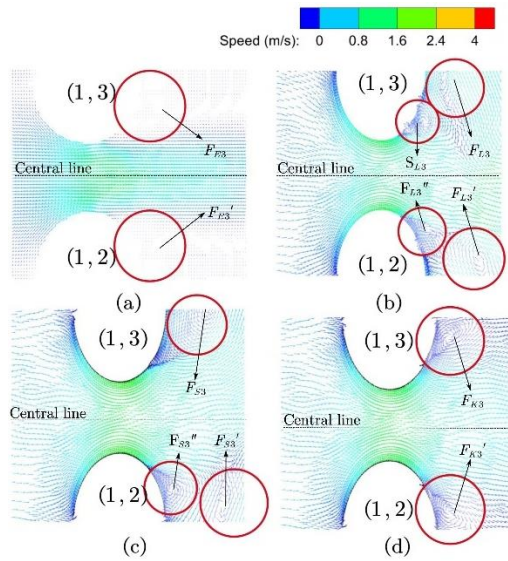
Fig. 9. Area around (1, 2) and (1, 3) velocity vector comparison between the experimental results (a) , laminar model results (b), S-A model (c), and standard *k-ε* model (d) at *Q* 5000μL/min.
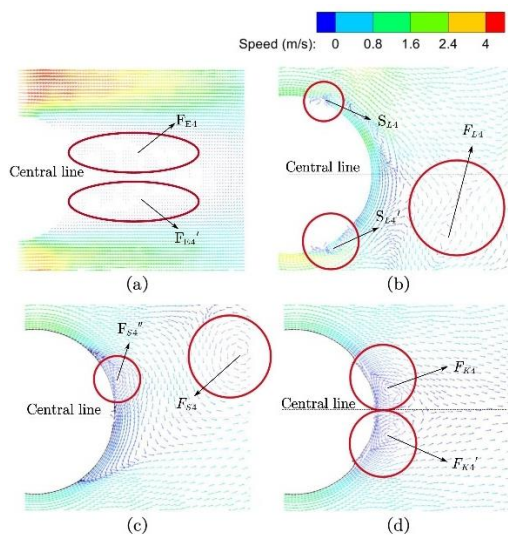

Fig. 10. Area downstream (6, 3) velocity vector comparison between the experimental results (a), laminar model results (b), S-A model (c), and standard *k-ε* model (d) at Q 8000μL/min.

conditions of *Q* 5000μL/min and 8000μL/min, respectively. The experimental results of these two figures show that the time-averaged velocity of the cylindrical wake zone is still symmetrically distributed about the center horizontal line, the velocity downstream of the cylinder near the wall is the lowest, and the velocity in the middle of the two cylinders is the highest.   When the flow rate reaches 5000μL/min, the flow separation phenomenon begins to occur downstream of the cylinder, and a pair of symmetrical mature foci are formed. With an increasing flow rate, the foci are narrower and longer. Simultaneously, the length of the wake

region increases, and the separation angle of the vortex becomes larger.

From Fig. 9(b), 10(b), 9(c) and 10(c), it can be seen that the time-averaged velocities of both the laminar flow model results and the S-A model results do not show symmetrical distribution. In Fig. 9 (b), a secondary vortex F$_{L3}$" adhering to the surface appears downstream of the cylinder (1, 2), as does a regular core that has been shed in the wake region. A secondary saddle point S$_{L3}$ with adhering walls appears downstream of cylinder (1, 3) and a narrow irregular focus is formed downstream. A symmetrical pair of wall-adhering secondary saddle points S$_{L4}$ and S$_{L4}$' appear downstream of the cylinder (6, 3) and form a dislodged foci F$_{L4}$ below the horizontal line of the cylinder center. The upper part of the wake region of cylinder (1, 2) is similar to the upper part of the wake region of cylinder (6, 3), and a wall-adhering secondary vortex appears downstream, F$_{S3}$. The *k-ε* model results are very similar at *Q* of 5000μL/min and 8000μL/min, with the difference that the focus downstream of the former is not shed, while the focus downstream of the latter has been dislodged. Both generate a pair of symmetrical focal points, F$_{K3}$ and F$_{K3}$', F$_{K4}$ and F$_{K4}$', downstream of the cylinder, and a saddle point appears. By comparing the four kinds of results under the two operating conditions, it can be found that the standard *k-ε* model results are more similar to the experimental results.

By comparing the time-averaged velocity vector plots, it can be noted that the results of the three numerical calculation models used in this paper are all somewhat different from the experimental results. Although the numerical models cannot match precisely the experimental results, choosing a numerical model that is closer to the experimental results is one feasible method. By determining the relationship between the degree of flow separation and the Re number, the standard *k-ε* model is closer to the experimental results at the four inlet flows.

4.3 Velocity Distribution Along Horizontal Gap Center Line

This section presents research on the velocity distribution along the horizontal gap center line. For ease of description, the horizontal gap center line between (1, 2) and (1, 3) is referred to as the (1, 2) horizontal line. So, in Fig. 11, A-B is the (1, 2) horizontal line. Figure 11 shows the relative velocity values of the (1, 2) horizontal line obtained using the laminar flow model, the S-A model and the standard *k-ε* model under the working conditions of
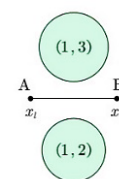

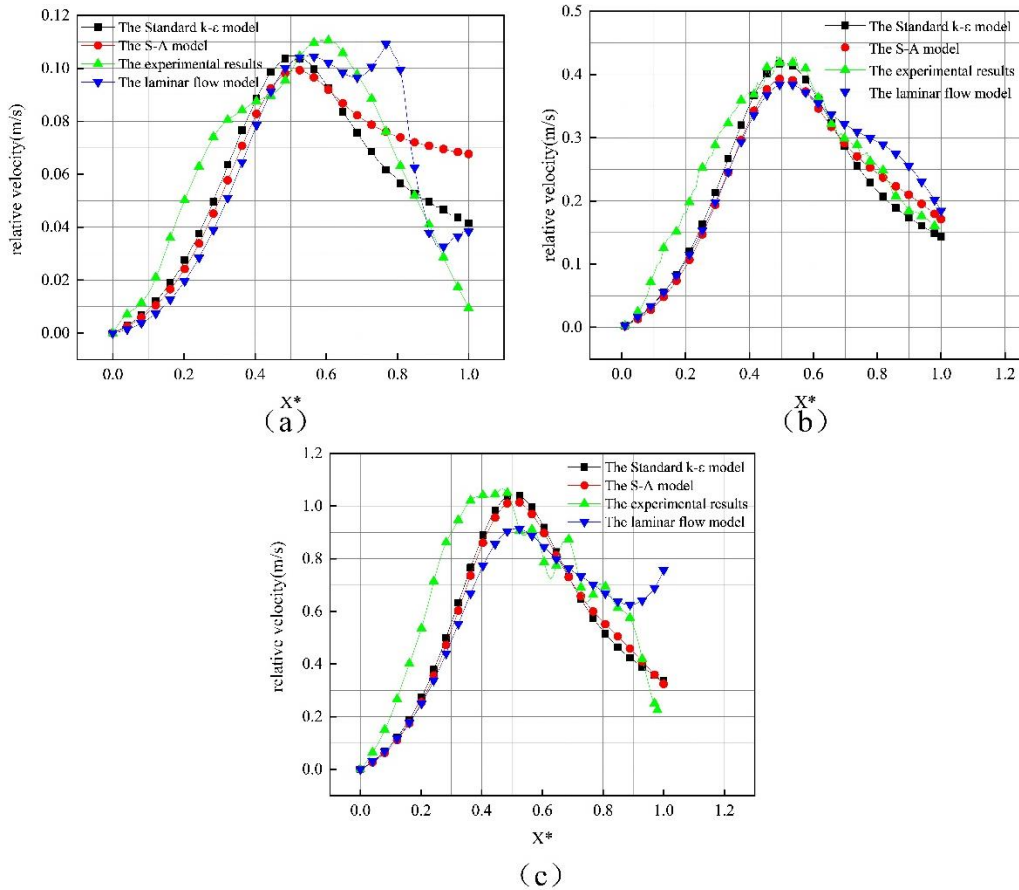**Fig. 11. Schematic diagram of a horizontal gap center line**.

Fig. 12. Relative velocity along (1, 2) horizontal line: a comparison between the laminar model, S-A model, standard *k-ε* model, and experimental results at (a) *Q* 500μL/min, (b) 2000μL/min, and (c) 5000μL/min

500μL/min, 2000μL/min and 5000μL/min, respectively. The simulation results were compared with the experimental results. The horizontal coordinate X* is the dimensionless variable, and calculated as follows:

$$X^{*} = \frac{x - x_{l}}{x_{r} - x_{l}} \tag{27}$$

In this formula, x_l is the location of point A, and x_r is the location of point B. Relative speed, the difference between the speed value of each point and the speed of point A, was adopted for this analysis. This was mainly because the field of view was limited during the Micro-PIV experiment, and the channel needed to be moved manually. Therefore, there is a degree of error in the location during movement, resulting in deviations in the data extracted from the target position during post-processing.

It can be seen from Fig. 12 that the relative speed of the four kinds of models is consistent in its overall trend. The results of the three numerical model results coincide in the first half. The maximum value, which occurs at X*, is 0.5, which is to be expected since X* 0.5 is the narrowest region. However, the models show significant differences in the second half. Especially the laminar model, when Q is 500μL/min and 2000μL/min, respectively, the

results are not decreasing monotonically at this stage; rather, there is a small range of ascent first, and then a descent. This is illogical. For the S-A model and standard *k-ε* model, these numerical results follow the trend.

There is observed difference between the experimental results and the numerical calculation results, as manifested in Fig. 12. Apart from the relative velocity magnitude, another difference is the shift of the point where maximum relative velocity occurs. For *Q* 500μL/min, this point is shift to upstream while for Q 5000, this point is shift to downstream. These differences are triggered by the manual movement of micro channel, resulting calibration deviation. By analyzing the accuracy and rationality, both S-A model and standard *k-ε* model are able to predict the velocity distribution a horizontal gap center line to some extents.

5. CONCLUSION

The present study was designed to study the flow pattern inside micro tube bank models and evaluate the numerical accuracy of the laminar model, the S-A model, and the standard *k-ε* model. First, a Micro-PIV system was used to measure the velocity distribution inside micro tube bank models at different inlet flow rates. Secondly, numerical

calculations based on the laminar flow model, the S-A model, and the standard k-ε model were conduct to predict the velocity distribution. Finally, an analysis of the numerical result accuracy was performed, and the differences between experimental and numerical results were compared to evaluate numerical accuracy. The main conclusions are as follows:

1) From the results of Micro-PIV, when Q starts from 3000μL/min, vortices begin to appear in the circular downstream area, and as the inlet flow increases, the vortices become more pronounced and the vortex length gradually increases.

2) From the numerical calculation results, it can be noted that the velocity distributions obtained by the laminar flow model, the S-A model, and the standard k-ε model are noticeably different. In terms of the velocity distribution along the horizontal gap center line, the results from the S-A model and the standard k-ε model results are logical while laminar flow model results are il logical. The three types of numerical results are close to the experimental results.

3) In terms of the vortex, clear differences exist between experimental results and the three types of numerical results. The standard k-ε model is better able to predict the vortex than the other two numerical models. This means standard k-ε model can be employed to analyze the fluid flow across a micro tube bank model to some extents.

REFERENCES

Ambreen, T. and M. H. Kim (2018). Effect of fin shape on the thermal performance of nanofluid-cooled micro pin-fin heat sinks. *International Journal of Heat & Mass Transfer* 126, 245-256.

Armellini, A., L. Casarsa and P. Giannattasio (2010). Low reynolds number flow in rectangular cooling channels provided with low aspect ratio pin fins. *International Journal of Heat and Fluid Flow* 31, 689-701.

Cai, L., G. Xia and H. Wang (2016). Parametric study on thermal and hydraulic characteristics of laminar flow in microchannel heat sink with fan-shaped ribs on sidewalls – Part 1. *Heat transfer* 97, 1069-1080.

Ejaz, F., W. Pao and H. M. Ali (2022). Numerical investigation and prediction of phase separation in diverging T-junction. *International Journal of Numerical Methods for Heat & Fluid Flow* 32(12), 3671-3696.

Hosseinizadeh, S. F., F. L. Tan and S. M. Moosania (2011). Experimental and numerical studies on performance of PCM-based heat sink with different configurations of internal fins. *Applied Thermal Engineering* 31, 3827-3838.

Ji, C., M. Lv, J. Huang, L. Duan and Z. Liu (2021). Experimental study on flow around a single pin fin in a microchannel. *Journal of Engineering Thermophysics* 42, 1844-1850.

Jia, Y., G. Xia, Y. Li, D. Ma and B. Cai (2018). Heat transfer and fluid flow characteristics of combined microchannel with cone-shaped micro pin fins. *International Communications in Heat & Mass Transfer* 92, 78-89.

Kumar, A., R. Kothari, S. K. Sahu and S. I. Kundalwal (2021a). A comparative study and optimization of phase change material based heat sinks for thermal management of electronic components. *Journal of Energy Storage* 43, 103224.

Kumar, A., R. Kothari, S. K. Sahu and S. I. Kundalwal (2021b). Thermal performance of heat sink using nano-enhanced phase change material (NePCM) for cooling of electronic components. *Microelectronics Reliability* 121, 114144.

Lee, K. B., M. Wilson and M. Vahdati (2018). Validation of a numerical model for predicting stalled flows in a low-speed fan--part i: modification of spalart- allmaras turbulence model. *Journal of Turbomachinery* 140, 1-11.

Li, J., C. Ji, Z. Liu, H. Li, C. Ma and W. Shi (2020). Experimental study on flow characteristics in a microchannel with a single cylinder. *Shandong Science* 33, 53-62.

Li, Y., M. Lv, Z. Liu and Y. Zhu (2018). Experimental study on flow past micro-cylinder-groups by Micro-PIV method. *Shandong Science* 31, 50-54.

Liu, Z., K. Dong, M. Lv, C. Ji and Y. Jiang (2021). Study on characteristics of flow field in micro pin fin array based on Micro-PIV. *CIESC Journal* 72, 5094-5101.

Liu, Z., M. Lv, L. Kong, L. Jia and Y, Jiang (2019), Study on flow field in micro-cylinder groups with different cross-section shapes by Micro-PIV method. *Shandong Science* 32, 81-87.

Paramanantham, S. S. S., V. M. Nagulapati and H. Lim (2022). Numerical investigation of the influence of microchannel geometry on the droplet generation process. *Journal of Applied Fluid Mechanics* 15(5), 1291-1305.

Qin, L., J. Hua, X. Zhao, Y. Zhu, D. Li and Z. Liu (2019). Micro-PIV and numerical study on influence of vortex on flow and heat transfer performance in micro arrays. *Applied Thermal Engineering* 161,114186.

Renfer, A., M. K. Tiwari, T. Brunschwiler, B. Michel and D. Poulikakos (2011). Experimental investigation into vortex structure and pressure drop across microcavities in 3D integrated electronics. *Experiments in Fluids* 51, 731-741.

Saravanan, V. and C. K. Umesh. (2018) Numerical comparison for thermo-hydraulic performance of pin fin heat sink with micro channel pin fin heat sink. *Sadhana-Academy Proceedings in Engineering Sciences* 43, 100.

Shafeie, H., O. Abouali, K. Jafarpur and G. Ahmadi (2013). Numerical study of heat transfer performance of single-phase heat sinks with micro pin-fin structures. *Applied Thermal Engineering* 58, 68-76.

Shah, T. R., H. M. Ali., C. Zhou, H. Babar, M. M. Janjua, M. H. Doranehgard, A. Hussain, U. Sajiad. C. C. Wang and M. Sultan (2022). Potential evaluation of water-based ferric oxide (Fe2O3-water) nanocoolant: An experimental study. *Energy* 246, 123441.

Shaheed, R., A. Mohammadian, H. Kheirkhah and G. Hossein. (2019) A comparison of standard k–ε and realizable k–ε turbulence models in curved and confluent channels. *Environmental Fluid Mechanics* 19, 543-568.

Siddiqui, M., M. A. Azam and H. M. Ali (2022). Parametric evaluation of condensate water yield from plain finned tube heat exchangers in atmospheric water generation. *Arabian Journal for Science and Engineering* 47, 16251-16271.

Stogiannis, I. A., A. D. Passos, A. A. Mouza, S. V. Paras, V. Pěnkavováb and J. Tihonb (2014). Flow investigation in a microchannel with a flow disturbing rib. *Chemical Engineering Science* 119, 65-76.

Tan, Y. F., M. H. Liu, Y. C. Kang, X. L. Wang and J. B. Liu (2017). Investigation into brush seal vortex separation point based on 2D staggered tube bundle model. *Journal of drainage and irrigation machinery engineering* 35(7), 602-608

Wang, K., J. Q. Liu, Z. C. Liu, W. Chen, X. C. Li and L. Zhang (2021). Fluid flow and heat transfer characteristics investigation in the shell side of the branch baffle heat exchanger. *Journal of Applied Fluid Mechanics* 14 (6), 1775-1786.

Wang, Y., F. Houshmand, D. Elcock and Y. Peles (2020). Convective heat transfer and mixing enhancement in a microchannel with a pillar. *International Journal of Heat and Mass Transfer* 62,553-561.

Xu, J., Y. Gan, D. Zhou and X. Li (2005). Microscale heat transfer enhancement using thermal boundary layer redeveloping concept. *International Journal of Heat and Mass Transfer* 48, 1662-1674.

Zhu, Y., N. Guan, D. Li, X. Zhao and Z. Liu (2017). Convection heat transfer characteristics of super-hydrophobic micro pin-fins with different cross-sectional shapes. *CIESC Journal* 68, 63-71.